Diyala Journal of Engineering Sciences

Journal homepage: https://djes.info/index.php/djes

ISSN: 1999-8716 (Print); 2616-6909 (Online)

Performance Analysis of Solar Air Heaters with Dimpled Roughness in Equilateral Triangular Ducts

Hadeel A. Hamed, Ammar A. Farhan*

Department of Energy Engineering, University of Baghdad, 10071 Baghdad, Iraq

ARTICLE INFO

Article history:
Received December 09, 2024
Revised January 25, 2025
Accepted February 12, 2025
Available online September 01, 2025

Keywords:
Solar air heater,
Dimple-shaped,
Performance enhancement criteria,
Artificial roughness,
Triangular duct.

ABSTRACT

Solar air heaters (SAHs) offer a practical and environmentally friendly method of harnessing solar energy. Enhancing the thermal performance of SAHs is critical, and various techniques, including surface modifications, have been explored. This experimental study investigates the influence of dimpled rib roughness on the thermal and hydraulic performance of a SAH with an equilateral triangular duct. The experiments were conducted over a range of operating conditions: relative roughness height (e/D) from 0.023 to 0.058, relative roughness pitch (L/e) from 3 to 9, relative roughness width (S/e) from 6 to 18, and Reynolds numbers from 6000 to 18000. The results indicate that the dimpled rib configuration significantly enhances heat transfer compared to smooth SAH. The maximum enhancement in the Nusselt number (Nu) and friction factor (f) is 5.78 and 2.26 times higher, respectively, than the smooth SAH. The highest performance enhancement criteria (PEC) value of 4.64 is achieved at e/D=0.058, L/e=3, and S/e=6. Additionally, empirical correlations for Nu and f were derived based on experimental data, providing valuable tools for SAH design optimization. This study demonstrates the potential of dimpled ribs to significantly improve SAH performance, making it a viable option for efficient solar energy utilization.

1. Introduction

The massive increase in global industry has resulted in unprecedented energy consumption. According to the current advances, power consumption will continue to climb significantly, tripling by 2060 [1]. Hence, due to increasing energy demand and environmental concerns, researchers are driven to explore more effective ways to harness green energy sources, including solar power and other renewable options [2]. Solar energy is one of the most abundant renewable resources available in nature, making it a highly popular choice among green energy sources due to its vast availability. Solar energy is primarily utilized for heating and electricity generation. Solar air heaters (SAHs) are employed to convert insolation into useful heat [3]. These devices use air as the working fluid, which is circulated either through natural convection or forced convection methods. SAHs are particularly effective in harnessing solar irradiance for space heating, drying agricultural products, and preheating ventilation air [4,5]. However, their primary drawback is low thermal efficiency, mainly caused by the poor coefficient of heat transfer between the air and the absorbing plate. To address this,

* Corresponding author.
E-mail address: ammarali@uobaghdad.edu.iq
DOI: 10.24237/djes.2025.18313

researchers have employed numerous techniques to augment heat transfer from the absorbing plate while balancing the increased power consumption required to keep airflow across the duct. Among these methods, using rib-roughness on the absorbing plate is the most prevalent [6,7]. Additionally, efficiency improvements have also been pursued by incorporating extended surfaces and different corrugation patterns beneath the absorbering plate [8].

Researchers aiming to boost the thermal and hydraulic performance of SAHs have utilized both numerical and experimental methods. Generally, these efforts focus on developing a new generation of SAHs with high thermal efficiency while reducing pressure drop due to airflow resistance. Tanda [9], experimentally examined the performance of SAHs using various rib arrangements (discrete V-shaped, angled continuous, transverse continuous, and broken) on the absorbing plate. The performance comparison of these various rib configurations, based on heat transfer and pressure drop, was examined to evaluate the characteristics of each rib arrangement at different Reynolds numbers. Karim and Hawlader [10] conducted both experimental and theoretical evaluations of three types of SAHs - flat, fined, and v-corrugated - under diverse climatic conditions. Their findings revealed that the v-corrugated collector operates with higher thermal efficiency compared to conventional flat and fined collectors. Creating synthetic roughness on the absorbing plate surface is seen as one of the most effective and cost-efficient ways to improve both the thermal and overall efficiency of SAHs. While providing roughness on the absorbing plate improves the heat transfer rate, it increases the pressure drop, requiring additional pumping power. Therefore, system parameters need to be optimized to maximize the heat transfer rate whilst to minimize the pressure drop [11]. Yang et al. [12] carried out experimental studies and numerical modeling to optimize the design of SAH with offset rectangular fins. They tested the thermal performance of the SAH by considering numerous parameters such as thermal efficiency, angle of incidence, time constant, and the coefficient of resistance. The findings indicated that under typical space heating conditions, even at low airflow rates, the thermal efficiency exceeded 40%. Kumar and Kim [13] presented numerical simulations and developed mathematical models to optimize SAH with various roughness shapes on the absorbing plate. They aimed to predict thermal and effective efficiencies based on heat transfer and friction factor correlations. Their study included various rib shapes such as V-rib, W-rib, discrete, transverse, angled, and multiple configurations. The findings indicated that SAH with discrete multiple V-shaped ribs on the absorbing plate achieved significant enhancements in thermal and effective efficiency compared to other rib shapes. The influence of the V-down rib geometrical parameters, including relative height (e/D) (0.019–0.043), relative pitch (p/e) (6–12), angles of attack (α) (30–75°), and Reynolds number (Re) (1000–20,000), on the SAH performance having triangular duct was studied numerically and real weather conditions data were used for validation. The data revealed that the thermal efficiency of the roughened SAH by V-down ribs exceeded that of the smooth SAH by 15.7% [14]. Hegde et. al [15] conducted a study on the energy and exergy performance of various V-shaped ribs in a SAH compared to a smooth SAH. The results indicate that the staggered multi-V rib achieved the highest thermal efficiency (76.63%). In comparison, the perforated multi-V rib demonstrated superior thermohydraulic efficiency (74.82%) and better exergy performance at higher Reynolds numbers. The V-groove SAH integrated with transverse wedge-shaped ribs (TWSR) demonstrated clear advantages over smooth SAHs under identical operating conditions. Farhan et al. [16] implemented a numerical investigation on an SAH roughened by TWSR and found a notable improvement in heat gain, and a 9.6% increase in thermal-hydraulic efficiency compared to a smooth SAH. Experimental tests on a solar thermal collector duct with a hybrid rib pattern (combining V-shaped and arc-shaped ribs) showed significant improvements in heat transfer and reduced friction. The innovative design enhances overall

thermal performance [17]. Mund et al. [18] examined the impact of stepped transverse ribs on the thermal performance of a solar air heater (SAH). Their findings revealed that the peak thermohydraulic performance parameter was 19.49% greater than that of a smooth SAH.

Dimple-shaped roughness significantly improved heat transfer between the airflow and the absorbing plate inside the SAH, with a smaller increase in pumping power penalties compared to other types of roughness. This improvement is attributed to the simple fabrication of spherical indentations and the fact that no extra weight is added to the absorbing plate [19]. Moon et al. [20] examined how the height of the channel influences heat transfer and friction factors in a dimpled channel. They found that the thermal efficiency of the dimpled channel outperformed that of continuous ribs. Saini and Verma [21] conducted a comprehensive experimental study to assess the influence of dimple-shaped coarseness on the performance of an SAH. Their findings indicated that the Nu and *f* were considerably influenced by the flow and roughness parameters. An SAH with an absorber plate roughened by dimple shapes arranged in an arc configuration has been investigated experimentally by Sethi et.al [22]. They noticed a significant enhancement in both Nu and *f*. An experimental and numerical investigation was carried out to predict the heat transfer and flow behavior of a triangular SAH with a dimpled absorbing plate. The results showed that the Nu for the roughened SAH was 5.33 times greater than that of the smooth SAH [23]. A SAH with an equilateral triangular duct demonstrated superior performance compared to one with a rectangular duct. This improvement refers to the increased contact area between the absorbing plate and the working fluid.

Existing research demonstrates that the performance of solar air heaters (SAHs) can be significantly enhanced by incorporating dimpled rib geometries on the absorber plate. However, there remains a need for a more comprehensive understanding of how these geometries influence airflow and heat transfer characteristics within equilateral triangular ducts. In particular, the effects of staggered dimpled ribs, which have the potential to induce secondary flows and enhance turbulence, are not well understood. This study aims to address these gaps by evaluating the heat transfer augmentation and the associated pressure loss penalty introduced by staggered dimpled rib geometries in comparison to smooth SAHs with equilateral triangular ducts. Furthermore, it seeks to determine the optimal configuration of these ribs, including the relative roughness height, pitch, and width, to achieve maximum thermal performance while minimizing pressure losses. An in-depth analysis of the flow dynamics is also conducted to understand the role of secondary flows and turbulence in improving heat transfer. Finally, the performance of the proposed staggered dimpled rib geometry is compared with existing roughness techniques to validate its effectiveness and demonstrate its potential for practical applications.

2. Roughness geometry

The SAH having an equilateral triangular duct is designed with a Vee corrugated absorbing plate with a flat back plate as shown in Figure 1. Due to the symmetry of the triangular channel, one channel is examined in the present work. The staggered rib pattern roughening the Vee corrugated absorbing plate is depicted in Figure 2. The detailed schematic diagram and pictorial view of staggered dimpled ribs have been shown in Figurs 2a and 2b. Several parameters must be adjusted to examine the influence of staggered dimpled roughness on the performance of the SAH. The relative roughness height, represented by the e/D (the ratio between dimple height (e) to the hydraulic diameter (D)), varies from 0.023 to 0.058. The pitch distance (L) which is the center distance between two adjacent ribs in the flow direction, is measured in terms of the relative roughness pitch, denoted by the L/e, ranges from 3 to 9. The transverse distance (S) which is the center distance between two adjacent ribs perpendicular to the flow direction, is measured in terms of the relative roughness width, expressed by the S/e, varies from 6 to 18. The relative roughness diameter (e/d) value, which are the ratio of the

dimple height (e) to the dimple print diameter (d), is 0.5. Experimental work has been implemented for Reynolds number (Re) in turbulent flow regions, ranging from 6000 to 18000. The variation of flow and roughness parameters of the current experimental study is shown in Table 1. The experimental findings from the present work include several performance criteria such as Nu, *f*, and PEC.

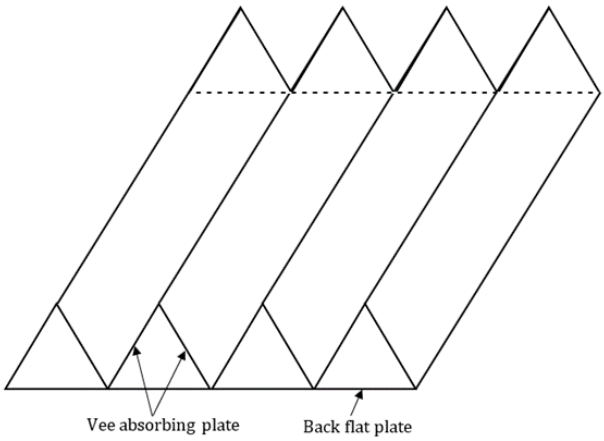

Figure 1. Schematic diagram for the SAH having equilateral triangular duct.

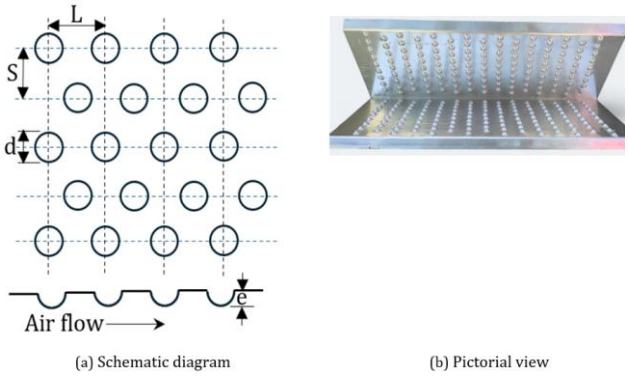

Figure 2. Staggered dimpled shape roughness.

Table 1: Investigated parameters in the present study.

S. No.	Parameters	Range
1	Re	6000-18000
2	e/D	0.023-0.058
3	L/e	3-9
4	S/e	6-18
5	e/d	0.5

3. Experimental setup

The indoor experimental setup shown in Fig. 3 was constructed to implement a comparative thermal investigation between the dimpled and smooth SAH with an equilateral triangular duct. An aluminum metal sheet with a thickness of 2 mm was used to construct the equilateral triangular duct, which has a side length of 150 mm. The test rig consists of three sections: an entrance section, a test section, and an exit section, with lengths of 900 mm, 500 mm, and 400 mm, respectively. The upper side of the Vee absorbing plate is covered by an electric heater constructed with nichrome wire on an asbestos sheet to provide controlled heating, while the back flat plate side is kept insulated An electrical variac arrangement has been linked to the heater to control the applied heat flux. A 50 mm thick glass wool insulation with 25 mm wooden ply is applied to decrease heat loss from the test section. A variable-speed air blower is used to circulate air inside the duct and regulate the air flow rate through the duct. The experiments were conducted under turbulent flow conditions with Re varying from 6000 to 18000. A honeycomb air distributor was installed inside the inlet section, 50 mm from the beginning of the test section, to maintain a uniform and smooth airflow inside the duct.

Thirteen K-type thermocouples, each 0.5 mm in diameter with an accuracy of ±1%, were used to measure the temperature distribution across the SAH. Five thermocouples were fastened on each side of the Vee absorbing plate, and three thermocouples were used to measure the inlet air, outlet air, and ambient temperature. An Applent 32-channel RS485 data logger (AT4532) was used to record the thermocouple readings. Figure 4 shows the temperature measuring points across the SAH. The pressure difference through the collector was gauged by a transmitter differential pressure and flow (SIEMENS SITRANS P DS III/P410), having an uncertainty level of ±0.04%, and an anemometer (TESTO 435), having an uncertainty level of ±3%, was used to measure the air velocity inside the duct.

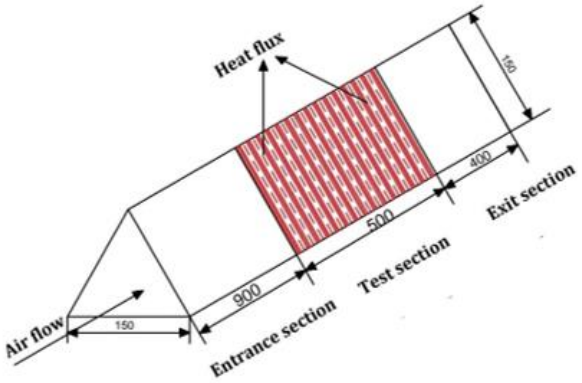

(a) A schematic diagram of the SAH with equilateral triangular duct(all dimensions in mm)

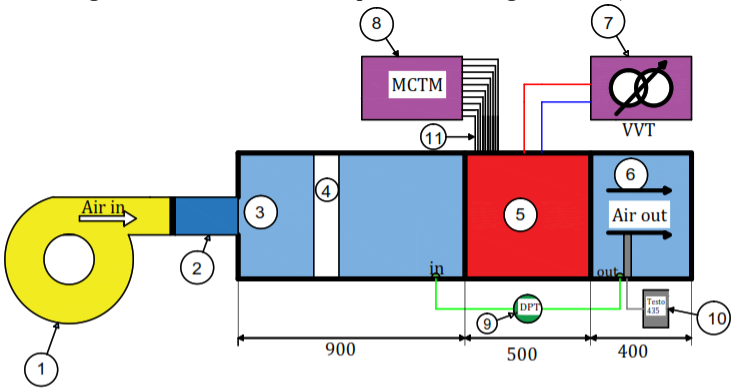

1- Blower	7- Variable Voltage Transformer 220 v
2- Flexible Pipe	8- Multi-channel Temperature Meter
3- Entry Section	9- Differential Pressure Transmitter
4- Honeycomb	10- Multi-function measuring instrument
5- Test Section	11- Thermocouple wire
6- Exit Section	(All Dimensions In mm)

(b) Details view of the test rig

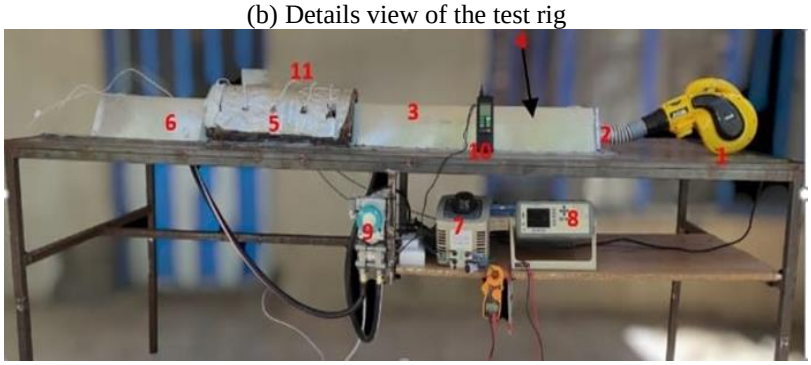

(c) Pictorial view of the SAH with equilateral triangular duct.

Figure. 3 A schematic diagram and experimental image of the test rig.

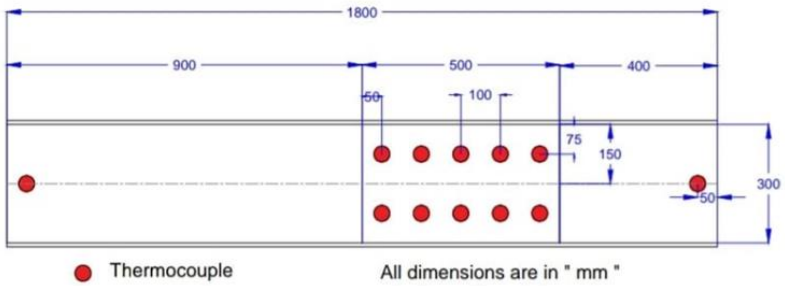

Figure 4. Location of the thermocouples on the absorber plate.

4. Data reduction

Energy absorbed by air flows under the absorbing plate, known as useful energy (Q_{use} in W), can be written as follows [24]

$$Q_{use} = \dot{m}_a \, c_p \left(T_{fo} - T_{fi}\right) \quad (1)$$

where $\dot{m}_a$, c_p, T_{fo}, and T_{fi} are air mass flowrate (kg/s), specific heat at constant pressure (J/kg/K), outlet air temperature (K), and inlet air temperature (K), respectively.

The average air temperature (T_f) can be calculated by

$$T_f = \frac{T_{fi}+T_{fo}}{2} \quad (2)$$

The average absorbing plate temperature can be calculated by

$$T_p = \frac{1}{10} \sum_{i=1}^{10} T_i \quad (3)$$

Reynolds number across the SAH is evaluated by the following equation [11]

$$Re = \frac{\rho v D}{\mu} \quad (4)$$

where ρ, v, D, and μ are air density (kg/m^3), air velocity (m/s), Hydraulic diameter (m), and dynamic viscosity (Pa.s), respectively. The hydraulic diameter for an equilateral triangular duct is computed as follows

$$D = \frac{4A}{P} = \frac{2a}{\sqrt{3}} \quad (5)$$

Where a (m) is the length of the equilateral triangle.

The average convection heat transfer coefficient between the absorbing plate and flowing air is computed as follows [25]

$$h = \frac{Q_{use}}{A_p \left(T_p - T_f\right)} \quad (6)$$

Nusselt number is calculated by the following formula.

$$Nu = \frac{hD}{k} \quad (7)$$

Where k is the thermal conductivity (W/m/K) of the air.

The friction factor is estimated by the following expression [11]

$$f = \frac{D\Delta P}{2L_d \, v^2 \rho} \quad (8)$$

4.1 Uncertainty Analysis

Experimental investigation needs uncertainty analysis to detect errors and uncertainties caused by humans and instruments to approve the validity of trial readings. Root-sum-square methodology suggested by Kline and McClintock [26] was adopted to estimate the uncertainties of the experimental data as follows

$$\frac{\delta y}{y} = \sqrt{\sum_{i=1}^{n} \frac{\partial y}{\partial x_i} \delta x_i} \quad (9)$$

Where y, x, and n are the dependent variable, independent variable, and the variable affecting the measurement, respectively. Based on the above equation, the calculations of uncertainty analysis for the Nu, Re, and f are as follows

$$Nu = \frac{hD}{k} \quad (10)$$

$$\frac{\delta Nu}{Nu} = \sqrt{\left(\frac{\delta h}{h}\right)^2 + \left(\frac{\delta D}{D}\right)^2 + \left(\frac{\delta k}{k}\right)^2} \quad (11)$$

$$Re = \frac{\rho v D}{\mu} \quad (12)$$

$$\frac{\delta Re}{Re} = \sqrt{\left(\frac{\delta \rho}{\rho}\right)^2 + \left(\frac{\delta v}{v}\right)^2 + \left(\frac{\delta D}{D}\right)^2 + \left(\frac{\delta \mu}{\mu}\right)^2} \quad (13)$$

$$f = \frac{D\Delta P}{2Lv^2\rho} \quad (14)$$

$$\frac{\delta f}{f} = \sqrt{\left(\frac{\delta D}{D}\right)^2 + \left(\frac{\delta \Delta P}{\Delta P}\right)^2 + \left(\frac{\delta L}{L}\right)^2 + \left(\frac{\delta v}{v}\right)^2 + \left(\frac{\delta \rho}{\rho}\right)^2} \quad (15)$$

The uncertainty values of Nu, Re, and f are 4.28%, 3.5%, and 4.52%, respectively.

4.2 Validation of experimental data

The anticipated values of the Nusselt number and friction factor, respectively, derived from the Dittus–Boelter equation and modified Blasius equation of the smooth duct, were compared to the Nusselt number and friction factor computed from the experimental data for the smooth duct[27].

Dittus–Boelter equation.

$$Nu_s = 0.023 \, Re^{0.8} Pr^{0.4} \quad (16)$$

f_s for a smooth duct is provided by the Blasius equation adjusted as:

$$f_s = 0.316 \, Re^{-0.25} \quad (17)$$

root mean squared error (RMSE) was computed as suggested by[28] , to evaluate the percentage error between the present results and those in other published work.

$$RMSE = \sqrt{\frac{\sum_1^n \left(X_{sim,i} - X_{exp,i}\right)^2}{n}} \quad (18)$$

Where $X_{exp,i}$, $X_{sim,i}$, and n are the experimental data, simulated data, and the number of data, respectively. *RMSE* are equal to zero for ideal cases.

Figure 5 and 6, respectively, compare the estimated and experimental results of Nu_s and f_s as a function of Re. It was discovered that the maximum deviation for the f_s was 3.6% and the maximum deviation for the Nu_s was 3.7%.

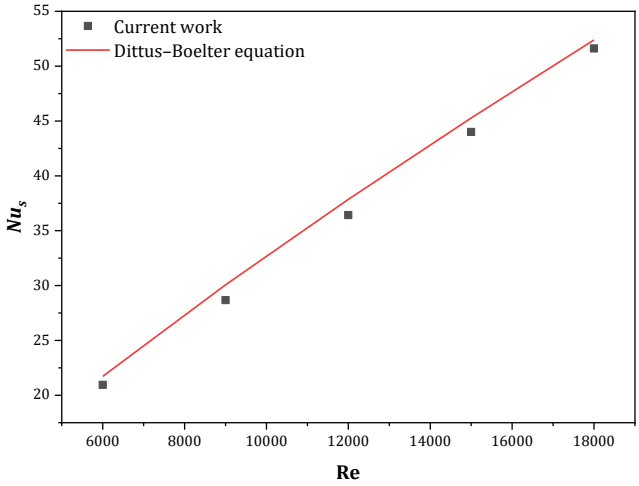

Figure 5. Comparison of experimental and predicted data of Nu_s.

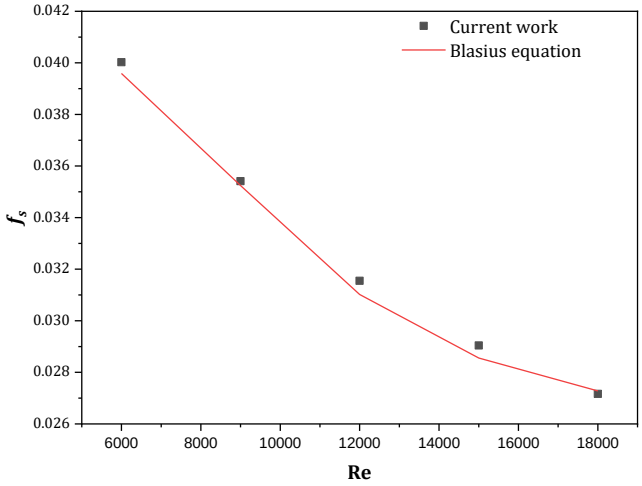

Figure 6. Comparison of experimental and predicted data of f_s

5. Results and discussion

In this section, the impact of roughness parameters and Re on Nu and f in an equilateral triangular duct is discussed in detail. The Nu and f are calculated based on the experimental data collected from smooth and dimpled SAHs.

5.1 Heat transfer characteristics

5.1.1 Impact of relative roughness height (e/D)

The variation of Nu as a function of Re for a range of e/D values is presented in Figure 7. Different e/D values of 0.023, 0.035, 0.046, and 0.058, with constant values of L/e=3 and S/e=6, are shown. The findings indicate that, for a given Re, the Nu values for the dimpled absorbing plate are much greater than those for the smooth one, demonstrating the enhancement in heat transfer due to the roughness elements.

As e/D increases, the height of the dimples grows, leading to more pronounced turbulence and greater disruption of the thermal boundary layer. This increase in turbulence enhances the mixing of cooler mainstream air with the heated boundary layer, resulting in higher heat transfer rates. Additionally, the dimples create flow separation and reattachment zones, which generate secondary flows and vortices. These vortices promote effective heat transfer by increasing the heat exchange surface area and enhancing the convective heat transfer coefficient. At an e/D of 0.058, the maximum Nu is observed. Beyond this point, further increases in e/D may lead to excessive pressure drop and diminishing returns in heat transfer. The low coefficient of heat transfer at the leading edge and the high coefficient at the trailing edge of the dimples highlight the role of reattachment in localized enhancement.

5.1.2 Impact of relative roughness pitch (L/e)

Figure 8 illustrates the effect of L/e values (3, 5, 7, and 9) on Nu over a Reynolds number range of 6000–18000, with other parameters (e/D=0.058 and S/e=6) held constant. The results show that for all L/e values, the roughened absorbing plate consistently exhibits significantly higher Nu values compared to the smooth plate. As L/e increases, the spacing between successive dimples widens, reducing the number of reattachment points on the absorbing plate. This reduction in reattachment points decreases the intensity of secondary flows and the associated disruption of the thermal boundary layer, leading to a decline in heat transfer. Smaller L/e values, such as L/e=3, produce more frequent and intense reattachment zones, which enhance turbulence and facilitate better heat transfer.

At L/e=, the highest Nu is observed at Re=18000. This can be attributed to the optimal balance between dimple density and flow disturbance. Higher values of L/e, while reducing the pressure drop penalty, fail to create sufficient turbulence for enhanced heat transfer.

These findings are consistent with previous studies, which indicate that tighter spacing between roughness elements generally results in better thermal performance. From an engineering perspective, optimizing L/e is crucial for achieving a trade-off between maximizing heat transfer and minimizing pressure losses, particularly in applications where energy efficiency is critical.

5.1.3 Impact of relative roughness width (S/e)

Figure 9 depicts the variation of Nu with Re for different S/e values (6, 9, 12, and 18), while e/D=0.058 and L/e=3 remain fixed. The findings reveal that Nu increases monotonously with increasing Re for all S/e values. However, at a given Re, Nu decreases linearly as S/e increases. This behavior is primarily due to the influence of S/e on the number and intensity of reattachment points. When S/e decreases, the dimples are spaced closer together, leading to the formation of larger and stronger vortices beneath the absorbing plate. These vortices disrupt the thermal boundary layer more effectively, facilitating greater heat transfer. Conversely, higher S/e values reduce the interaction between successive dimples, diminishing the turbulence and lowering the heat transfer enhancement.

The maximum Nu is achieved at S/e=6 and Re=18000, which corresponds to the optimal configuration for maximizing turbulence and reattachment. However, very small S/e values could lead to excessive pressure drop penalties, reducing the overall system efficiency. These results align with prior research indicating that smaller S/e values enhance heat transfer by intensifying vortex formation and flow disturbance. Practical applications of these findings suggest that careful optimization of S/e is necessary to ensure high thermal performance without incurring significant pressure losses.

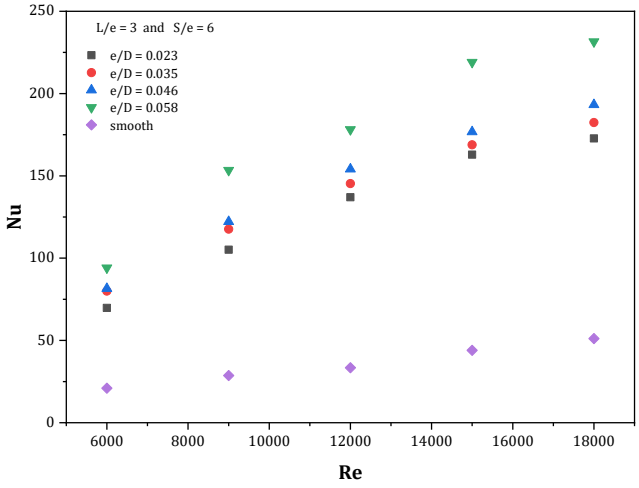

Figure 7. Variation of Nu with Re at distinct e/D.

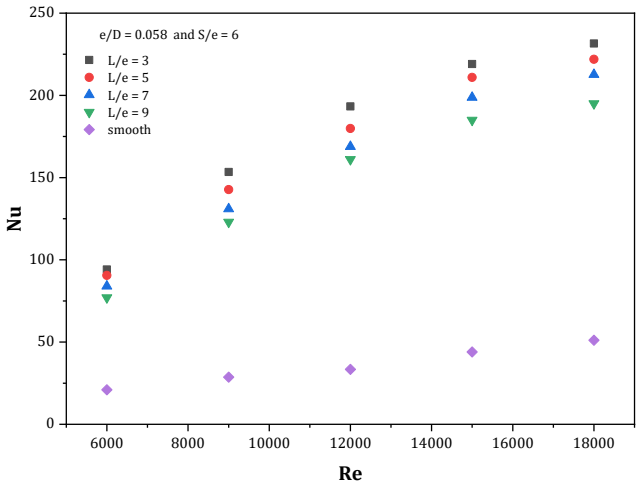

Figure 8. Variation of Nu with Re at distinct L/e.

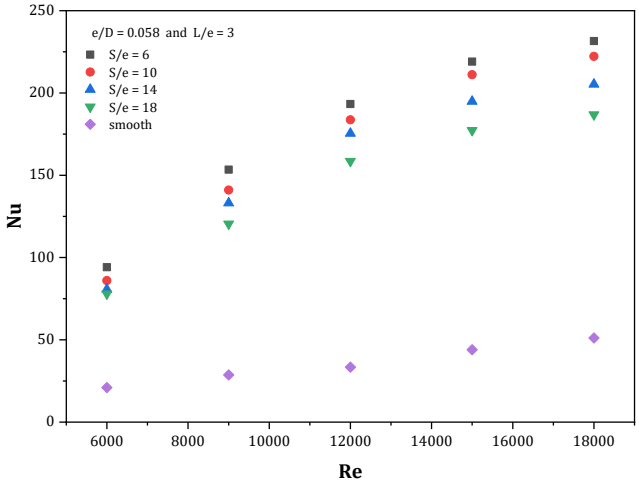

Figure 9. Variation of Nu with Re at distinct S/e.

5.2 Friction factor characteristics

5.2.1 Influence of relative roughness height (e/D)

The impact of fluid flow and roughness parameters on the friction factor is shown in Figurs 10-12. It has been noted that *f* decreases monotonously with the growth in Re due to the laminar sublayer suppression occurring inside the duct. Also, it can be observed that the *f* values of the dimpled absorbing plate are higher than those of the smooth absorbing plate. Figure 10 illustrates the effect of *f* as a function of Re for e/D values of 0.023, 0.035, 0.046, and 0.058 and for a fixed value of L/e and S/e of 3 and 6, respectively. The minimum value of *f* occurs at e/D of 0.023; this is because of the decrease in dimple height, which leads to the formation of a weak recirculation zone of the flow, which creates a weak secondary flow. As a result, less power is needed to move air through the duct, and vice versa.

5.2.2 Influence of relative roughness pitch (L/e)

Figure 11 depicts the variation of *f* with respect to Re for a fixed value of S/e and e/D, which are 6 and 0.058, respectively, and L/e values of 3, 5, 7, and 9. When L/e = 3, and a given Re value, *f* reaches its maximum value. This is due to an increased friction penalty because at L/e = 3, the maximum number of reattachment points is created. The friction cost decreases as the L/e increases because fewer dimples are present.

5.2.3 Influence of relative roughness width (S/e)

Similarly, the variation of *f* for different values of S/e has been plotted in Figure 12. The results indicate that the *f* value that corresponds to S/e = 6 is the maximum, and the f value that corresponds to S/e = 18 is the minimum. It belongs to the maximum dimples number come into contact with fluid flow at S/e is 6. Thus, the maximum number of created vortices required more pumping power to overcome the friction loss.

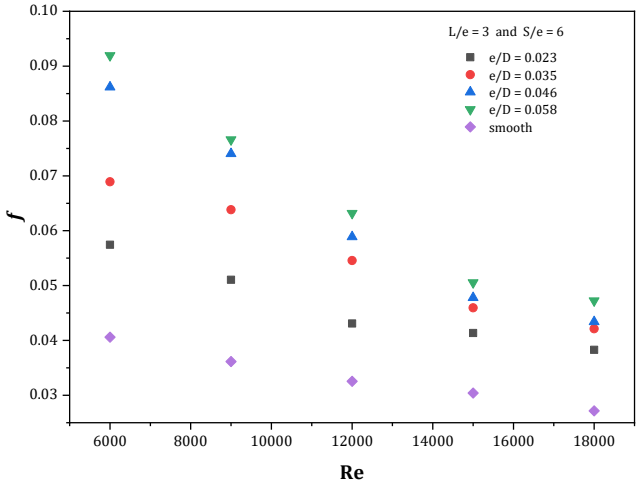

Figure 10. Variation of *f* with Re at distinct e/D.

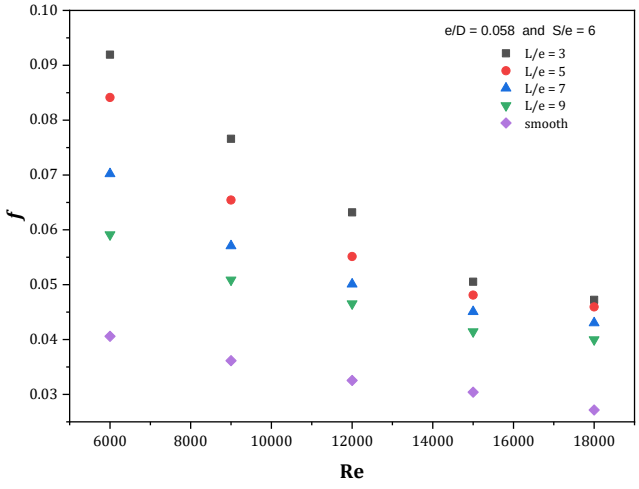

Figure 11. Variation of *f* with Re at distinct L/e.

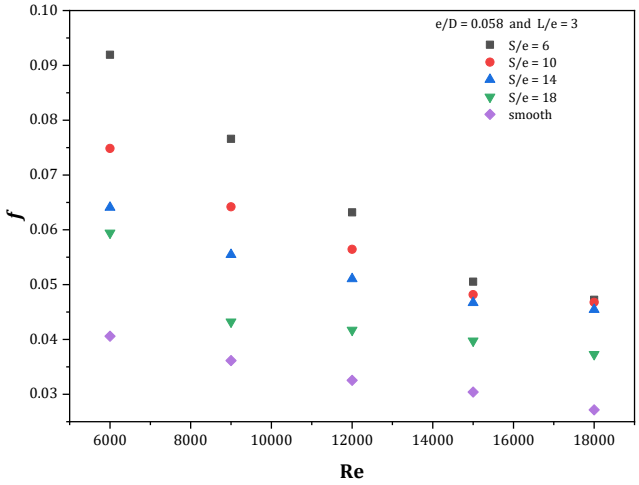

Figure 12. Variation of *f* with Re at distinct S/e.

5.3 Performance enhancement criteria (PEC)

In the current work, any enhancement in heat transfer between the airflow and the absorbing plate inside a solar air heater (SAH) is achieved at the expense of increased friction loss. The performance enhancement criterion (PEC)

serves as a tool to evaluate the trade-off between heat transfer augmentation and friction penalty, enabling the selection of optimal roughness parameters. This criterion is defined as the ratio of the Nusselt number (Nu) for the roughened SAH to that for the smooth one under identical pumping power conditions and is calculated as follows [29].

$$PEC = \frac{\frac{Nu_r}{Nu_s}}{\left(\frac{f_r}{f_s}\right)^{\frac{1}{3}}} \quad (19)$$

The numerator quantifies the improvement in convective heat transfer due to roughness, while the denominator accounts for the frictional losses introduced by the roughened surface.

Figurs 13–15 illustrate the variation of PEC with respect to the dimpled roughness parameters for different Reynolds numbers (Re). These figures reveal that the PEC increases with increasing Re up to Re = 12000, reaching a peak value, before decreasing linearly for Re > 12000. This trend is physically explained as follows: at low to moderate Re values, the turbulent eddies generated by the roughness elements enhance the convective heat transfer significantly while causing a relatively moderate increase in friction losses. However, at higher Re values, the increased velocity intensifies the frictional losses disproportionately compared to the gains in heat transfer, resulting in a net decline in PEC.

The results also indicate that the roughness geometry plays a crucial role in determining the PEC. Specifically, the combination of e/D= 0.058, L/e= 3, and S/e= 6 achieves a balance between heat transfer enhancement and frictional losses, yielding the best PEC. Physically, this combination likely optimizes the flow separation and reattachment process, maximizing the thermal boundary layer disruption while avoiding excessive pressure drops. In contrast, other configurations may either underperform in heat transfer augmentation or incur excessive friction penalties.

A detailed comparison of the PEC of the present work with the results from other available studies is depicted in Table 2. By examining these comparisons, the table illustrates how the current study's findings align with previously established research, thereby offering a comprehensive context for evaluating the SAH with an equilateral triangular duct roughened by a dimpled shape. The dimple rib geometry leads to the highest heat transfer rates in SAHs due to its unique ability to enhance turbulent flow while minimizing flow resistance in critical regions. Unlike traditional ribs or rectangular roughness elements, dimples act as localized turbulence promoters, creating a pattern of vortices and flow reattachment zones. These vortices disrupt the thermal boundary layer effectively, increasing the convective heat transfer from the absorber plate to the airflow.

Additionally, the concave nature of the dimples contributes to their efficiency by trapping small-scale eddies that sustain turbulence even at moderate Reynolds numbers, providing consistent heat transfer performance across a wide operating range. This contrasts with geometries like backward-chamfered or V-down ribs, which often rely on sharp edges and abrupt flow separation that can cause excessive pressure drops. In summary, the superior performance of the dimple rib geometry in the present study can be attributed to its ability to create a stable and effective turbulence-inducing mechanism while maintaining relatively low flow resistance compared to other roughness designs. This makes it particularly well-suited for enhancing the thermal performance of SAHs with minimal energy penalties.

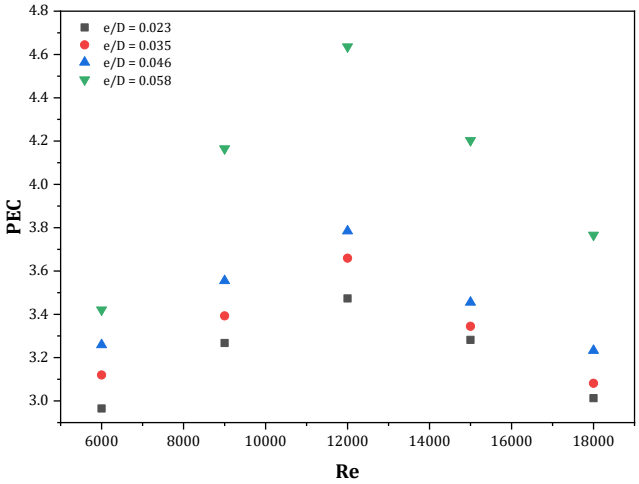

Figure 13. variation in PEC as a function of Re for various e/D values.

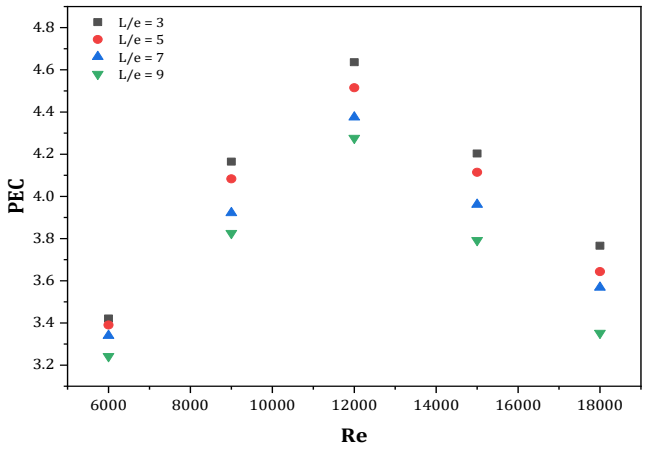

Figure 14. variation in PEC as a function of Re for various L/e values.

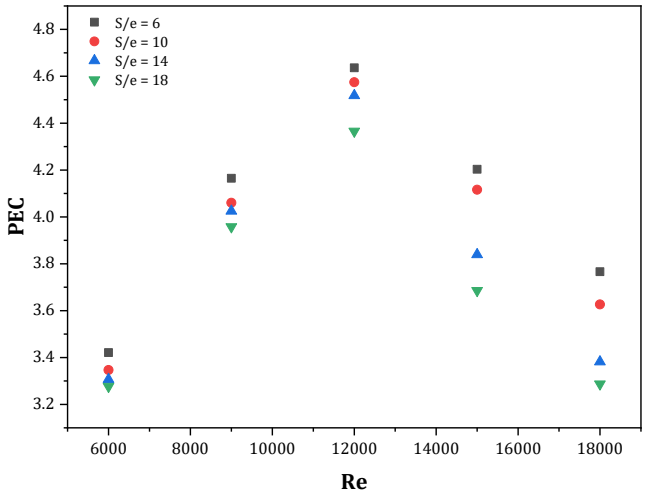

Figure15. variation in PEC as a function of Re for various S/e values.

Table 2: PEC of roughened SAH having a triangular duct.

Authors	Roughness geometry	Parameters	PEC
Bharadwaj et al.[30]	Inclined ribs	Re=4500-28000 , P/e=4-16 , e/D=0.021-0.043, α =30-75°.	4.38
Goel et al. [31]	hemispherical dimple-cavities that	Re=2100-18500 , x/r_d=6.4-14.7 , r_d/D=0.016-0.039, y/r_d =6.4-14.7	3.48
Kumar et al. [32]	forward-facing chamfered rectangular ribs	Re=4000-17000 , e/D=0.018-0.043 , e/w=0.24-1.5, e'/e =0-1	2.88
Kumar, Rajneesh Goel, Varun [33]	backward-chamfered rectangular-rib	Re=3700-18700, e/D=0.0433, P/e=11, e/w=0.67 and 2.	2.68
Misra et al. [34]	V-down ribs with multiple gaps	Re=4000-20000 P/e=8-14, α=45-60°, e/w = 0.25-4.	2.06
Kumar, Rajneesh Kumar, Anoop Goel, Varun[35]	Rectangular rib	Re=4000-18000 P/e=5-15, e/D=0.02-0.04, e/w = 0.25-4.	1.89
Present study	Dimple	Re=6000-18000, e/D=0.023-0.058, L/e=3-9, S/e=6-18.	4.64

6. Correlations for Nu and f

It is observed, as discussed in the previous section, that Nu and f are strongly influenced by the dimpled parameters and flow parameters, namely e/D, L/e, S/e, and Re. Therefore, the functional relationships for Nu and *f* can be expressed as follows:

Nu = Nu (Re ,e/D ,L/e ,S/e) (20)

f = *f* (Re, e/D, L/e , S/e) (21)

The mathematical expressions for Nu and f, derived from regression analysis, are shown below.

6.1 Nu correlation

The statistical correlations have been developed using a similar process to that employed in earlier published publications[36,37]. Figure 16

shows all experimental data points of Nu as a function of Re. It has been observed that Nu has a linear relationship with Re. A regression analysis is used to fit a straight-line equation through these points, represented as follows:

$$Nu = A_0 Re^{0.8313} \quad (22)$$

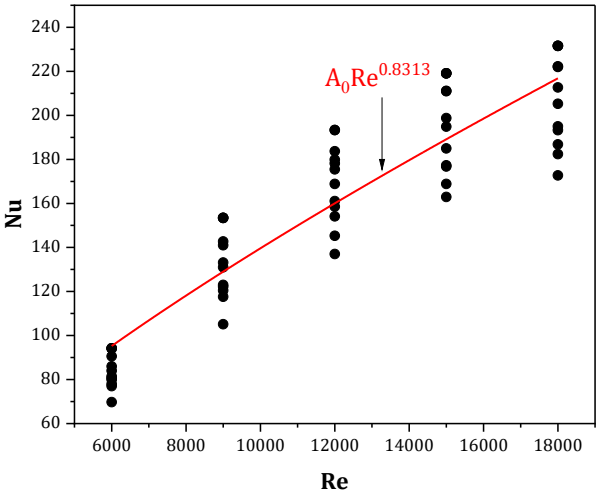

Figure 16. Variation of Nu with Re

Where A_0 will be a function of other parameters. By taking the parameter e/D into consideration, Fig. 17 is plotted between ($Nu/Re^{0.8313}$) and (e/D). A regression formula has been used to fit these points, which is given by

$$\frac{Nu}{Re^{0.8313}} = B_0 \times \left(\frac{e}{D}\right)^{0.3731} \quad (23)$$

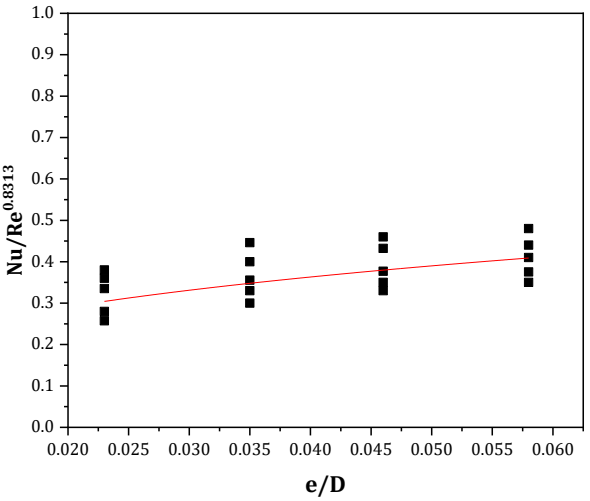

Figure 17. Plot of $Nu/Re^{0.8313}$ versus e/D

Where B_0 is a function of L/e and is plotted as shown in Figure 18. A regression analysis is performed on these points using a straight line fit, expressed by:

$$\frac{Nu}{Re^{0.8313}\left(\frac{e}{D}\right)^{0.3731}} = C_0 \left(\frac{L}{e}\right)^{-0.1312} \quad (24)$$

Where C_0 is a function of S/e. Similarly, C_0 is plotted against $Nu/(Re^{0.8313}\ (e/D)^{0.3731}\ (L/e)^{-0.1312})$ as depicted in Figure 19. A first-order fit is used to fit these points and is given by

$$\frac{Nu}{Re^{0.8313}\left(\frac{e}{D}\right)^{0.3731}\left(\frac{L}{e}\right)^{-0.1312}} = D_0 \left(\frac{S}{e}\right)^{-0.1473} \quad (25)$$

Where the value of D_0 is 0.312.

The final formula for Nu after integrating all the above values becomes

$$Nu = 0.312 \times Re^{0.8313} \times \left(\frac{e}{D}\right)^{0.3731} \times \left(\frac{L}{e}\right)^{-1312} \times \left(\frac{S}{e}\right)^{-0.1473} \quad (26)$$

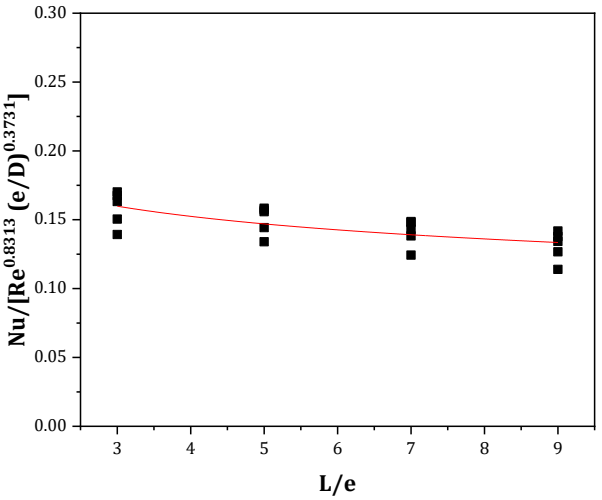

Figure 18. Plot of $Nu/[Re^{0.8313}\ (e/D)^{0.3731}]$ with (L/e)

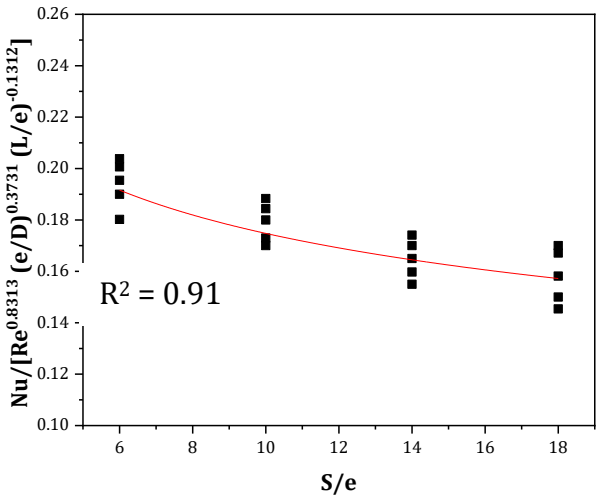

Figure 19. Plot of $Nu/[Re^{0.8313}\ (e/D)^{0.3731}\ (L/e)^{-0.1312}]$ versus (S/e)

6.2 Friction factor correlation

In a similar manner, the same procedure has been implemented to derive the friction factor correlation. Figures 20-23 depict the relationship between the friction factor, flow parameters, and roughness parameters. The final form of the derived correlation can be expressed as follows:

$$f = 46.2807\, Re^{-0.5037} \times \left(\frac{e}{D}\right)^{0.3616} \times \left(\frac{L}{e}\right)^{-0.2651} \times \left(\frac{S}{e}\right)^{-0.3076} \quad (27)$$

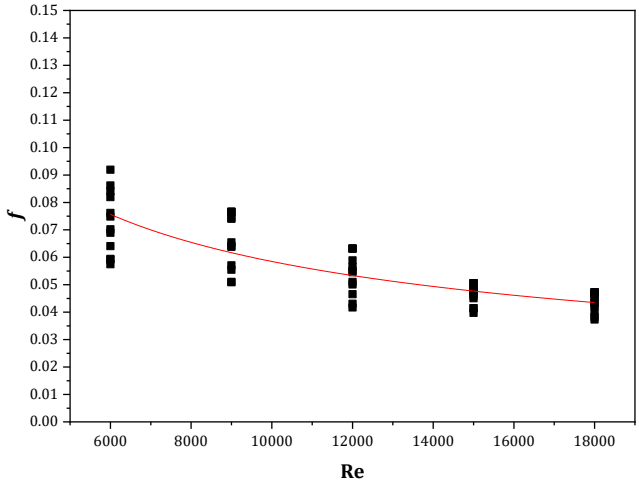

Figure 20. Variation of *f* with Re

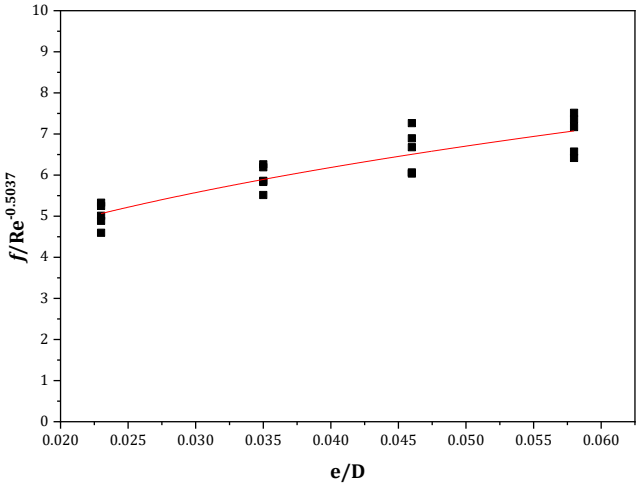

Figure 21. Plot of f/Re$^{-0.5037}$ versus e/D

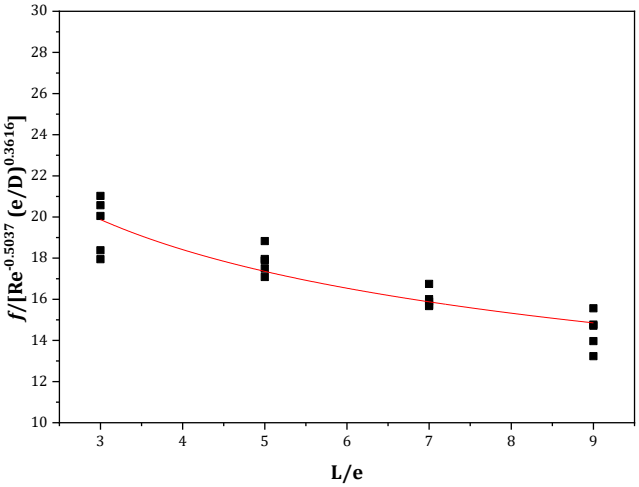

Figure 22. Plot of *f*/[Re$^{-0.5037}$ (e/D)$^{0.3616}$] with (L/e)

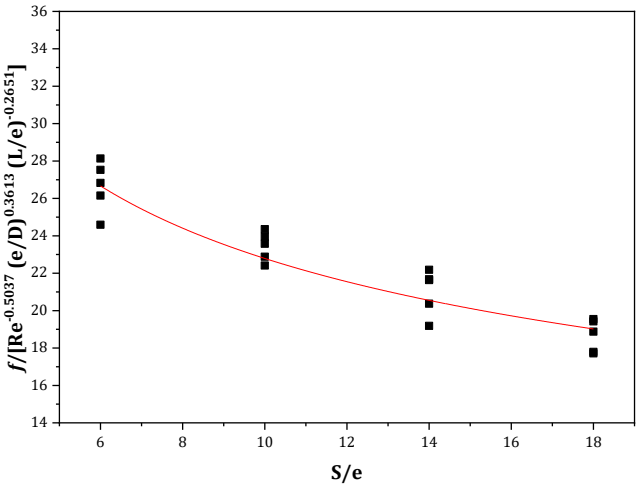

Figure 23. Plot of *f*/[Re$^{-0.5037}$ (e/D)$^{0.3616}$ (L/e)$^{-0.2651}$] versus (S/e)

The predicted values of the Nusselt number and friction factor, estimated by Eqs. 26 and 27, are plotted against the experimental data as shown in Figures 24 and 25. It can be seen that the deviation between the predicted and experimental values is ±11%, which is within an acceptable limit. It can be concluded that the predicted values of the Nusselt number and friction factor have reasonable precision using the correlations in Eqs. 26 and 27 for the range of investigated parameters.

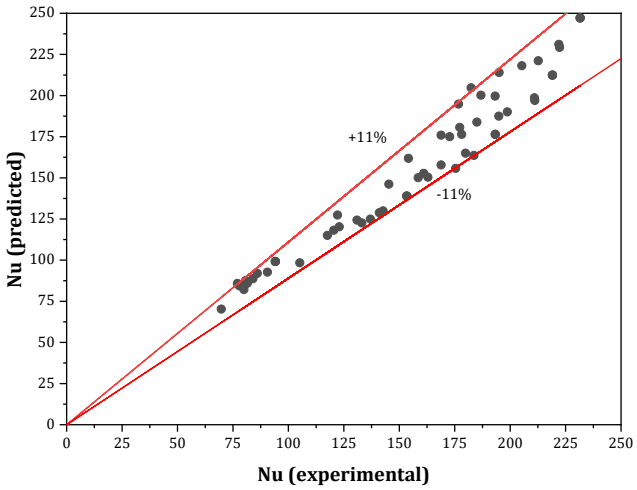

Figure 24. Plot of Nu (predicted) versus Nu (experimental).

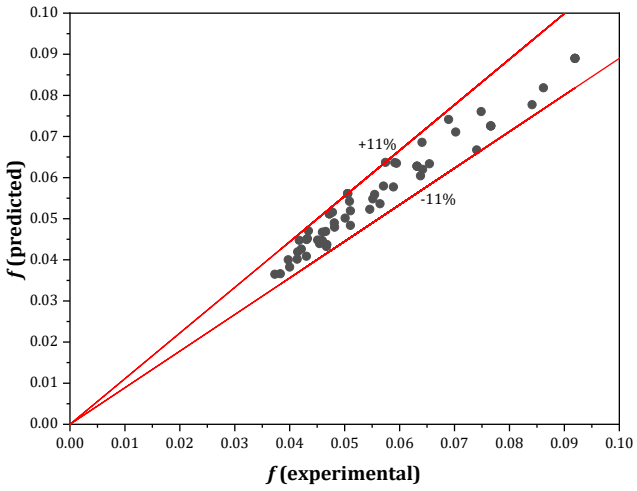

Figure 25. Comparison between predicated and experimental values of friction factor

7. Conclusions

An extensive experimental investigation was conducted to determine the impact of dimpled roughness on the performance of a solar air heater (SAH). Using an equilateral triangular duct roughened by staggered dimple ribs on the absorber plate, the study provided the following insights:

1. For all cases, increasing the Reynolds number (Re) enhanced the Nusselt number (Nu) while reducing the friction factor (*f*). This trend indicates improved thermal performance at higher flow rates but with a penalty in pressure loss. The roughened SAH consistently outperformed the smooth SAH in both heat transfer and flow resistance metrics.
2. Maximum enhancements in Nu and *f* of 5.78 and 2.26, respectively, were observed, underscoring the effectiveness of dimpled roughness in promoting turbulence and heat transfer. This improvement is significant for applications requiring high thermal efficiency, such as in regions with limited solar insolation.
3. The highest performance evaluation criterion (PEC) of 4.64 was achieved at the optimal combination of relative roughness height (e/D=0.058), relative roughness length (L/e=), relative roughness pitch (S/e=6), and Re=9000. This finding highlights the potential of dimpled roughness in maximizing energy efficiency under specific operating conditions.
4. Empirical correlations for Nu and *f* were derived based on flow and roughness parameters. These correlations provide a reliable tool for predicting the performance of similar systems and can aid engineers in designing more efficient SAHs. The maximum deviation of ±11% confirms the robustness and practical applicability of the derived models.
5. The findings indicate that incorporating dimpled roughness can significantly enhance the thermal performance of SAHs while maintaining reasonable pressure losses. This makes them viable for use in renewable energy systems, especially in industrial or residential applications where compact and efficient air heating systems are required.
6. Future research could focus on optimizing dimple geometry, exploring different working fluids, or testing under varying environmental conditions to expand the applicability of the proposed design.

Nomenclature

c_p	specific heat at constant pressure (J/kg/K)
d	dimple print diameter (m)
D	hydraulic diameter (m)
e	dimple height (m)
e/d	relative roughness diameter
e/D	relative roughness height
f	friction factor
h	heat transfer coefficient (W/m^2/K)

k	thermal conductivity (W/m/K)
L	pitch distance (m)
L/e	relative roughness pitch
L_d	duct length (m)
$\dot{m}$	air mass flowrate (kg/s)
Nu	Nusselt number
PEC	performance enhancement criteria
Q_{use}	useful energy (W/m^2)
Re	Reynolds number
RMSE	root mean square error
S	transverse distance (m)
S/e	relative roughness width
SAH	solar air heater
T_{fi}	average air temperature (K)
T_{fi}	inlet air temperature (K)
T_{fo}	outlet air temperature (K)
T_p	average absorbing plate temperature (K)
v	air velocity (m/s)

Greek symbols

ΔP	pressure drop (Pa)
ρ	air density (kg/m^3)
μ	air dynamic viscosity (Pa. s)

References

[1] M. A. Alfellag, H. E. Ahmed, M. G. Jehad, and A. A. Farhan, "The hydrothermal performance enhancement techniques of corrugated channels: a review," J Therm Anal Calorim, vol. 147, no. 19, pp. 10177–10206, Oct. 2022, doi: 10.1007/s10973-022-11247-1.

[2] A. M. Kadhim and I. M. Ali, "Experimental Evaluation of Evaporative Cooling for Enhancing Photovoltaic Panels Efficiency Using Underground Water," Journal of Engineering, vol. 26, no. 8, pp. 14–33, 2020, doi: 10.31026/j.eng.2020.08.02.

[3] A. Bhushan, R. Kumar, and A. Perwez, "Experimental investigations of thermal performance for flat and dimpled plate solar air heater under turbulent flow conditions," Solar Energy, vol. 231, no. November 2021, pp. 664–683, 2022, doi: 10.1016/j.solener.2021.11.060.

[4] S. Panda and R. Kumar, "Investigation of the effect of dimensional and non-dimensional parameters on the performance of pitch-varied staggered arranged dimple solar air heaters," Solar Energy, vol. 276, no. May, p. 112663, 2024, doi: 10.1016/j.solener.2024.112663.

[5] P. K. Mahto, P. P. Das, S. Diyaley, and B. Kundu, "Parametric optimization of solar air heaters with dimples on absorber plates using metaheuristic approaches," Appl Therm Eng, vol. 242, no. January, p. 122537, 2024, doi: 10.1016/j.applthermaleng.2024.122537.

[6] A. S. Yadav, S. Gupta, A. Agrawal, R. Saxena, N. Agrawal, and S. Nashine, "Performance enhancement of solar air heater by attaching artificial rib roughness on the absorber Plate," Mater Today Proc, May 2022, doi: 10.1016/J.MATPR.2022.05.064.

[7] M. M. Mahdi and A. A. Gaddoa, "Outdoor Testing of a Zig-Zag SolarAir heater with and without Artificial Roughness on Absorber Plate," Journal of Engineering, vol. 25, no. 4, pp. 1–17, 2019, doi: 10.31026/j.eng.2019.04.01.

[8] Y. F. Midhat and I. M. A. Aljubury, "Numerical Simulation of the Thermal Performance of a Tubular Solar Air Heater," Journal of Engineering, vol. 29, no. 11, pp. 143–166, 2023, doi: 10.31026/j.eng.2023.11.09.

[9] G. Tanda, "Performance of solar air heater ducts with different types of ribs on the absorber plate," Energy, vol. 36, no. 11, pp. 6651–6660, 2011, doi: https://doi.org/10.1016/j.energy.2011.08.043.

[10 M. A. Karim and M. N. A. Hawlader, "Performance investigation of flat plate , v-corrugated and finned air collectors," Energy, vol. 31, pp. 452–470, 2006, doi: 10.1016/j.energy.2005.03.007.

[11 A. A. Farhan, I. M. A. Aljubury, and H. E. Ahmed, "Energetic and exergetic efficiency analysis of a v-corrugated solar air heater integrated with twisted tape inserts," Renew Energy, vol. 169, pp. 1373–1385, 2021, doi: 10.1016/j.renene.2021.01.109.

[12 M. Yang, X. Yang, X. Li, Z. Wang, and P. Wang, "Design and optimization of a solar air heater with offset strip fin absorber plate," Appl Energy, vol. 113, pp. 1349–1362, 2014, doi: 10.1016/j.apenergy.2013.08.091.

[13 A. Kumar and M. H. Kim, "Numerical optimization of solar air heaters having different types of roughness shapes on the heated plate - Technical note," Energy, vol. 72, pp. 731–738, 2014, doi: 10.1016/j.energy.2014.05.100.

[14 M. Alaskari, A. M. Kadhim, A. A. Farhan, M. Al-Damook, and M. Al Qubeissi, "Performance Evaluation of Roughened Solar Air Heaters for Stretched Parameters," Clean Technologies, vol. 4, no. 2, pp. 555–569, 2022, doi: 10.3390/cleantechnol4020034.

[15] A. K. Hegde, R. Pai, and K. V. Karanth, "Influence of solar insolation on energy and exergy efficiency of a rectangular duct solar air heater with various types of V rib roughness: An analytical approach," International Communications in Heat and Mass Transfer, vol. 153, Apr. 2024, doi: 10.1016/j.icheatmasstransfer.2024.107397.

[16] A. A. Farhan, H. E. Ahmed, and M. A. Mussa, "Thermal–Hydraulic Performance of a V-Groove Solar Air Collector with Transverse Wedge-Shaped Ribs," Arab J Sci Eng, vol. 47, no. 7, pp. 8915–8930, 2022, doi: 10.1007/s13369-021-06442-5.

[17] T. Alam, "Development of correlations of Nusselt number and friction factor of solar thermal collector equipped with hybrid rib roughness," Solar Energy

Materials and Solar Cells, vol. 272, Aug. 2024, doi: 10.1016/j.solmat.2024.112887.

[18] C. Mund, S. Kumar Rathore, and R. Kumar Sahoo, "Experimental investigation of heat transfer augmentation of impinging jet solar air heater with stepped transverse ribs," Thermal Science and Engineering Progress, vol. 56, p. 103020, Dec. 2024, doi: 10.1016/j.tsep.2024.103020.

[19] B. Markam and S. Maiti, "Artificial enhancer for small-scale solar air heater—A comprehensive review," Cleaner Energy Systems, vol. 4, no. November 2022, p. 100046, 2023, doi: 10.1016/j.cles.2022.100046.

[20] H. K. Moon, T. O. O'Connell, and B. Glezer, "Channel height effect on heat transfer and friction in a dimpled passage," Transactions of ASME Journal of Gas Turbine and Power, vol. 122, no. 2, pp. 307–313, 2000.

[21] R. P. Saini and J. Verma, "Heat transfer and friction factor correlations for a duct having dimple-shape artificial roughness for solar air heaters," Energy, vol. 33, no. 8, pp. 1277–1287, 2008, doi: 10.1016/j.energy.2008.02.017.

[22] M. Sethi, N. S. Thakur, and Varun, "Heat transfer and friction characteristics of dimple-shaped roughness element arranged in angular fashion (arc) on the absorber plate of solar air heater," Journal of Renewable and Sustainable Energy, vol. 4, no. 2, 2012, doi: 10.1063/1.3700191.

[23 V. Goel, R. Kumar, S. Bhattacharyya, V. V. Tyagi, and A. M. Abusorrah, "A comprehensive parametric investigation of hemispherical cavities on thermal performance and flow-dynamics in the triangular-duct solar-assisted air-heater," Renew Energy, vol. 173, pp. 896–912, 2021, doi: 10.1016/j.renene.2021.04.006.

[24] S. S. Bhuvad, R. Azad, and A. Lanjewar, "Thermal performance analysis of apex-up discrete arc ribs solar air heater-an experimental study," Renew Energy, vol. 185, pp. 403–415, Feb. 2022, doi: 10.1016/j.renene.2021.12.037.

[25] S. Q. Hussien and A. A. Farhan, "The effect of metal foam fins on the thermo-hydraulic performance of a solar air heater," International Journal of Renewable Energy Research-IJRER, vol. 9, no. 2, pp. 840–847, Jul. 2019, [Online]. Available: https://www.ijrer.org/ijrer/index.php/ijrer/article/view/9276

[26] S. J. Kline and F. P. McClintock, "Describing uncertainties in single sample experiments," Mechanical Engineering, vol. 75, pp. 3–8, 1963.

[27 [27] J. A. Duffie, W. A. Beckman, and N. Blair, Solar Engineering of Thermal Processes, Photovoltaics and Wind, Fifth edit. JohnWiley& Sons, Inc., Hoboken,New Jersey, 2020.

[28 [28] H. Jarimi, M. N. Abu Bakar, M. Othman, and M. H. Din, "Bi-fluid photovoltaic/thermal (PV/T) solar collector: Experimental validation of a 2-D theoretical model," Renew Energy, vol. 85, pp. 1052–1067, 2016, doi: 10.1016/j.renene.2015.07.014.

[29 R. L. Webb, E. R. G. Eckert, and Rj. Goldstein, "Heat transfer and friction in tubes with repeated-rib roughness," Int J Heat Mass Transf, vol. 14, no. 4, pp. 601–617, 1971.

[30 G. Bharadwaj, Varun, R. Kumar, and A. Sharma, "Heat transfer augmentation and flow characteristics in ribbed triangular duct solar air heater: An experimental analysis," Int J Green Energy, vol. 14, no. 7, pp. 587–598, 2017, doi: 10.1080/15435075.2017.1307751.

[31 V. Goel, R. Kumar, S. Bhattacharyya, V. V. Tyagi, and A. M. Abusorrah, "A comprehensive parametric investigation of hemispherical cavities on thermal performance and flow-dynamics in the triangular-duct solar-assisted air-heater," Renew Energy, vol. 173, pp. 896–912, 2021, doi: 10.1016/j.renene.2021.04.006.

[32 R. Kumar, V. Goel, and A. Kumar, "Investigation of heat transfer augmentation and friction factor in triangular duct solar air heater due to forward facing chamfered rectangular ribs: A CFD based analysis," Renew Energy, vol. 115, pp. 824–835, 2018, doi: 10.1016/j.renene.2017.09.010.

[33 R. Kumar and V. Goel, "Unconventional solar air heater with triangular flow-passage: A CFD based comparative performance assessment of different cross-sectional rib-roughnesses," Renew Energy, vol. 172, pp. 1267–1278, 2021, doi: 10.1016/j.renene.2021.03.068.

[34 R. Misra et al., "Prediction of behavior of triangular solar air heater duct using V-down rib with multiple gaps and turbulence promoters as artificial roughness: A CFD analysis," Int J Heat Mass Transf, vol. 162, p. 120376, 2020, doi: 10.1016/j.ijheatmasstransfer.2020.120376.

[35R. Kumar, A. Kumar, and V. Goel, "A parametric analysis of rectangular rib roughened triangular duct solar air heater using computational fluid dynamics," Solar Energy, vol. 157, pp. 1095–1107, Nov. 2017, doi: 10.1016/j.solener.2017.08.071.

[36] R. P. Saini and J. S. Saini, "Heat transfer and friction factor correlations for artificially roughened ducts with expanded metal mesh as roughness element," Int J Heat Mass Transf, vol. 40, no. 4, pp. 973–986, 1997.

[37] T. Alam, R. P. Saini, and J. S. Saini, "Effect of circularity of perforation holes in V-shaped blockages on heat transfer and friction characteristics of rectangular solar air heater duct," Energy Convers Manag, vol. 86, pp. 952–963, 2014.